Solvent-Controlled Charge Storage Mechanisms of Spinel Oxide Electrodes in Mg Organohaloaluminate Electrolytes

Lu Wang,[†] Zhaohui Wang,[†,‡] Per Erik Vullum,[‡,§] Sverre M. Selbach,[†] Ann Mari Svensson,[†] and Fride Vullum-Bruer[,†]*

[†]Department of Materials Science and Engineering, Norwegian University of Science and Technology, NO-7491 Trondheim, Norway

[‡]SINTEF Materials and Chemistry, 7491 Trondheim, Norway

[§]Department of Physics, Norwegian University of Science and Technology, 7491 Trondheim, Norway

*E-mail: fride.vullum-bruer@ntnu.no

ABSTRACT: Considering the improved safety, reduced cost and high volumetric energy density associated with Mg batteries, this technology has distinct advantages for large-scale energy storage compared to other existing battery technologies. However, the divalency of the Mg^{2+} cation cause sluggish magnesiation kinetics in crystalline host materials, resulting in poor performance with regards to capacity and cycling stability for intercalation based electrodes. Here, we present a Mg battery using Mn_3O_4 as the electrode material and Mg metal as the counter electrode in a Mg organohaloaluminate electrolyte. The reversible capacity when Mn_3O_4 was used as cathode reached ~580 mAh g^{-1} at a current density of 15.4 mA g^{-1}, while a reversible capacity of ~1800 mAh g^{-1} was obtained in an anode configuration. The Mn_3O_4 in a cathode configuration shows excellent cycling stability, with no loss of capacity after 500 cycles at a current density of 770 mA g^{-1}. As an anode, Mn_3O_4 retained 86% of its initial capacity after 200 cycles. These exceptional charge storage properties and high cycling stability are attributed to highly reversible interfacial reactions involving the electrolyte solvents. Our conclusions are supported by density functional theory (DFT) calculations in addition to quantitative kinetics analysis and scanning transmission electron microscopy (STEM) combined with energy dispersive spectroscopy (EDS) and electron energy loss spectroscopy (EELS).

KEYWORDS: Mn_3O_4, Mg organohaloaluminate electrolyte, reversible interfacial reactions, electrolyte solvents, quantitative kinetics analysis

Rechargeable Mg batteries using Mg metal as counter electrode have attracted more and more attention as promising candidates for heavy load applications, such as electric vehicles, due to the advantages of Mg metal in terms of safety and cost.[1-3] However, the development of Mg batteries is far from reaching the success of Li batteries due to the high charge density of the Mg cation, which results in sluggish diffusion kinetics in host lattices.[1,2] There are only a few compounds developed so far, which meet the reversible intercalation/de-intercalation criteria of Mg cations. Most of these are sulfides (*e.g.* Mo_6S_8,[4,5] MoS_2,[6,7] Ti_2S_4[8]) and oxides (*e.g.* MoO_3,[9,10] V_2O_5[11,12]). Unfortunately, either moderate capacities or poor cycling stabilities were obtained from these intercalation-based electrode materials. Thus, it is quite urgent to find new approaches, which are able to circumvent these issues limiting the development of Mg batteries. One effective strategy is the utilization of a cell system where the capacity originates from electrode/electrolyte interfacial reactions rather than from Mg intercalation. Similar charge storage mechanisms have been successfully achieved in other rechargeable batteries. For example, the capacity obtained in nano-sized electrode materials for Li batteries, like Nb_2O_5[13] and TiO_2[14], is found to be based mostly on capacitive processes, and thus provide significantly enhanced capacities according to Dunn *et al.*.[13-15] By taking the advantage of the capacitive effect, Shen *et al.* also obtained an improved capacity in SnS/graphene composites used as anode electrode in Na batteries.[16] Among the published studies on Mg batteries, several research groups report capacitive-governed charge storage mechanisms in electrodes for Mg batteries as well.[17-19] However, none of them show particularly stable cycling performance. The exception is one paper previously published by our group,[20] which shows high capacity, excellent rate performance and long term stability of Mn_3O_4 cathodes in an all phenyl complex (APC)-tetrahydrofuran (THF) electrolyte. These exceptional properties are attributed to a combination of capacitive charge/discharge in combination with

reversible interfacial reactions involving the electrolyte species. This capacitive mechanism mainly comes from partial desolvation of the Mg complexes at the interface of the Mn_3O_4 cathode and APC-THF electrolyte. During the magnesiation process in the APC-THF electrolyte, the Mg cations from the Mg metal counter electrode are first solvated by the surrounding chlorine ions and THF molecules to form Mg dimers-$[Mg_2(\mu\text{-}Cl)_3 \cdot 6THF]^+$,which is the species responsible for the transport of Mg cations in the bulk of the Mg organohaloaluminate electrolyte.[3,21,22] When these Mg dimers approach the electrode/electrolyte interface they decompose to Mg monomers-$[MgCl \cdot 5THF]^+$.[22,23] Canepa *et al.*[23] strongly suggests that three coordinated THF molecules in the Mg monomer can be readily removed with the assistance of the electrode surface, while the $[MgCl \cdot 2THF]^+$ strongly adsorbs at the electrode/electrolyte interface and is the relevant Mg complex involved in charge transfer across the interface.

The surface properties of the electrode determine the degree of desolvation of Mg complexes at the interface. For example, the Mg complex can be fully desolvated at the interface of the Mo_6S_8 electrode and APC electrolyte with the aid of the interaction between the Mo cations and the coordinated species of the Mg complex.[2,24,25] However, low degrees of desolvation of the Mg complexes have been reported for most metal oxides due to strong interactions between the Mg cations and the surrounding coordinated species,[2] like the Mn_3O_4-APC-THF cell system.[20] This most likely gives rise to partial desolvation of the Mg complexes at the electrode/electrolyte interface. Thus, the adsorption of this partially desolvated Mg complex on the electrode surface could provide a capacitive contribution, while the coordinated species may be involved in the interfacial reactions. Indeed the THF molecules coordinated with Mg cations are readily oxidized to γ-butyrolactone (GBL) at the electrode/electrolyte interface in the presence of RMg^+, which acts as a Lewis acid.[26,27] In addition, several side products may be co-formed during the THF-GBL

oxidation, like THF peroxide,[28,29] 2-hydroxytetrahydrofuran[30] and 2,2-dihydroxytetrahydrofuran[31]. The THF opening-derivatives,[27,30,32,33] like THF oligomers, might form as well at this interface. All of these potential interfacial reactions render the electrode/electrolyte interface more complex than the case is for Li-ion batteries, in line with the studies done by Aurbach *et al.*.[34] As a consequence, the complete understanding of the solvent-related interfacial reactions is still lacking due to the complexity of the APC electrolyte. In spite of this, based on the high cycling stabilities of the Mn_3O_4 cathode at both low and high current densities,[20] these reactions are found to be highly reversible. Recently, Song *et al.*[32] also indicated that the interfacial reactions involving the species of the APC electrolyte could provide a considerable capacity during cycling. It is well-known that the interfacial property, which determine the interfacial reactions in the Mn_3O_4-APC cell system, has a dramatic effect on the cell performance, since the transfer of the ions and electrons occur at this interface.[35] Utilizing interfacial reactions as a means of improving charge storage and performance of the Mn_3O_4 electrode is therefore a possibility which is explored in the work presented here.

In this work, we have performed a systematic study of the magnesiation mechanism in Mn_3O_4 nanoparticles in APC electrolyte. In combination with the DFT calculations and the experimental data from electrochemical measurements and STEM/EDS/EELS characterizations, the charge storage mechanism in the Mn_3O_4 nanoparticles in APC electrolyte with different electrolyte solvents has been further studied. Instead of Mg intercalation in Mn_3O_4 host, the capacity is confirmed to originate from the interfacial reactions occurring during cycling, which involved and is controlled by electrolyte solvents. Especially, in APC-1,2-dimethoxyethane (DME) electrolyte, the chemical nature of these interfacial reactions can be altered by the adjustment of the cut-off potentials. By shifting the cut-off potentials to lower values it was also found that Mn_3O_4

nanoparticles work well as anode material. The reversible capacities measured for both Mn_3O_4 cathode and Mn_3O_4 anode are to the best of our knowledge, the highest values reported for any Mg battery electrode materials (see comprehensive comparison in Table S1 and Table S2). These excellent electrochemical properties obtained from Mn_3O_4 electrodes enabled by reversible interfacial reactions could be a promising strategy for promoting the development of Mg batteries with both high capacity and high cycling stability.

RESULTS AND DISCUSSION

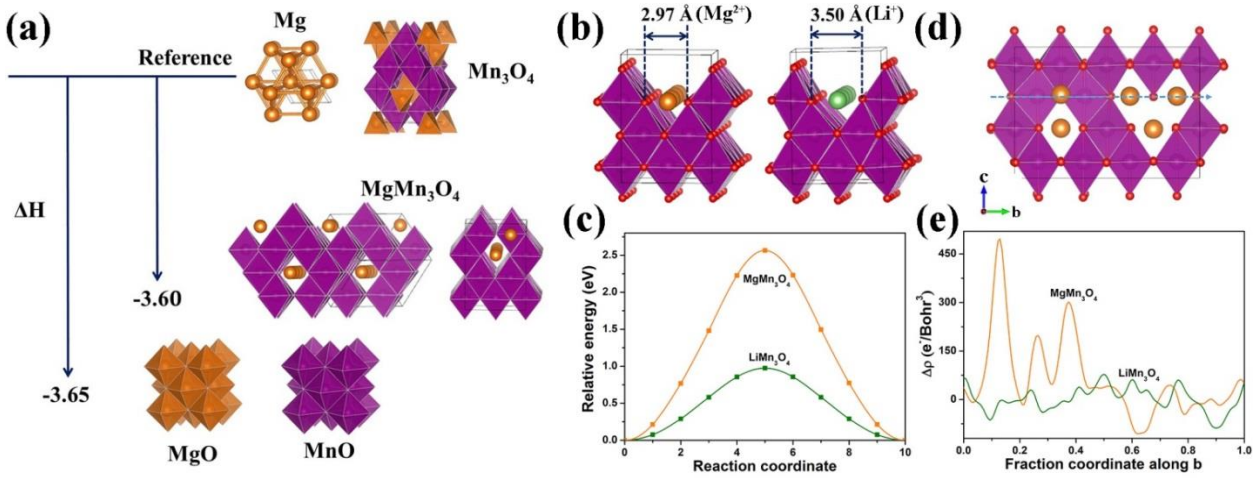

Figure 1. Energetics of the interaction between Mg cations and the Mn_3O_4 host. (a) Illustration of the calculated enthalpies (eV) of the Mg intercalation reaction (reaction 1) and conversion reaction (reaction 4) relative to a reference state with pure Mg and Mn_3O_4. (b) Illustration of the diffusion channels for vacancy defects in $MgMn_3O_4$ and $LiMn_3O_4$, consisting of edge-sharing octahedra. The top layer is removed for a better view of the diffusion channel. (c) Relative energies along the diffusion pathway for the Mg vacancy defects in $MgMn_3O_4$ and $LiMn_3O_4$. The points on the curve are the calculated values and the lines are spline fitting curves. (d) Saddle point structure for Mg

vacancy diffusion in $MgMn_3O_4$. (e) Planar charge difference ($\Delta\rho$ [e^-/Bohr^{-3}]) along the b-axis for the $MgMn_3O_4$ and $LiMn_3O_4$ supercells with a vacancy at the initial stat e and at the saddle point.

Energetics of the interaction between Mg cations and the Mn_3O_4 host. Mn_3O_4 displays a tetragonally deformed structure with space group $I4_1/amd$, where Mn^{2+} and Mn^{3+} occupy the tetragonal 4a and octahedral 8d Wyckoff sites, respectively. Jahn-Teller active high-spin d^4 Mn^{3+} causes a tetragonal elongation along the c-axis.[36,37] Possible intercalation sites of Mg cations into the spinel Mn_3O_4 are the unoccupied tetrahedral 4b sites and octahedral 8c sites. The Mg intercalation into 4b sites is however energetically unfavorable due to the positive formation energy. The intercalation voltage is -2.43 V vs. Mg^{2+}/Mg for the 4b site explicitly, (0, 0, ½) and (0, ½, ¾) at the charge limit, corresponding to insertion of one Mg into the $Mn_{12}O_{16}$ spinel structure. The likely intercalation sites for Mg cations are therefore the octahedral 8c positions. The intercalation voltage is 0.32 V vs. Mg^{2+}/Mg for all the four 8c positions, namely (0, ¼, ⅛), (½, ¼, ⅝), (¾, ½, ⅜) and (¾, 0, ⅞), which corresponds to inserting one Mg into a $Mn_{12}O_{16}$ spinel cell. When Mg cations intercalate into 8c sites, Mn^{2+} cations in the face-sharing tetragonal 4a positions will be pushed into a neighbouring octahedral 8c sites to reduce the total energy, resulting in a rock salt type structure at the discharge limit.[38] The 8c positions in the new rock salt structure are shared 50/50 by Mg and Mn cations.

The overall reaction of Mg intercalation into the spinel Mn_3O_4 lattice at discharge limit is expressed in reaction (1) below:

$$Mn_3O_4 + Mg^{2+} + 2e^- \leftrightarrow MgMn_3O_4 \qquad (1)$$

The internal energy of reaction (1) is estimated as

$$\Delta E_{f,int} = E_{MgMn3O4} - E_{Mn3O4} - E_{Mg} \qquad (2)$$

where $E_{MgMn3O4}$, E_{Mn3O4}, E_{Mg} are the ground state energies of the corresponding compounds. Since the pV term can be neglected, the enthalpy of formation can be expressed as

$$\Delta H_{f,int} = \Delta E_{f,int} + pV \approx \Delta E_{f,int} \quad (3)$$

The intercalation voltage can be calculated from

$$V_{int} \approx -\Delta H_{f,int} /2F \quad (4)$$

where F is the Faraday constant.

The overall conversion reaction for the electrode materials can be described by the following reaction:

$$Mn_3O_4 + Mg = MgO + 3MnO \quad (5)$$

The enthalpy of the conversion reaction can therefore be approximated as the internal energy change of the reaction

$$\Delta H_{conv} \approx \Delta E_{con} = E_{MgO} + 3E_{MnO} - E_{Mn3O4} - E_{Mg} \quad (6)$$

The conversion voltage can be expressed as

$$V_{conv} \approx -\Delta H_{conv} /2F \quad (7)$$

The calculated enthalpy of $MgMn_3O_4$ formation, i.e. the intercalation reaction (reaction 1) is -3.65 eV and enthalpy of the conversion reaction (reaction 5) is -3.60 eV. Correspondingly, the intercalation voltage (V_{int}) at the discharge limit is 1.83 V vs. Mg^{2+}/Mg and the conversion voltage (V_{conv}) is 1.80 V vs. Mg^{2+}/Mg. The energetics of the interaction between Mg cations and the Mn_3O_4 host relative to the reference state corresponding to bulk Mg and Mn_3O_4 are illustrated in Figure 1a. The negative formation energies indicate that both the interaction and conversion reactions can occur simultaneously at the cathode surface. As defined earlier by Canepa *et al.*, the competition

of the two reactions depends on the relative values of V_{int} and V_{conv}.[39] If $V_{conv} > V_{int}$, the conversion reaction is thermodynamically favored against the intercalation of Mg into the host material, and vice versa. Note that, in this study, the difference between V_{conv} and V_{int} is subtle for the Mn_3O_4 host materials, indicating that both reactions will compete at the cathode surface, unless one is hindered by kinetics, as addressed further below.

Compared with Li cations in the Mn_3O_4 host, the high charge density of the Mg cations causes shorter in-plane O-O bonds in the Mg/Li octahedral, resulting in a narrower diffusion channel (see Figure 1b; 2.97 and 3.50 Å for Mg and Li cations, respectively). The energetics of the in-plane diffusion pathways for a Mg vacancy defect in $MgMn_3O_4$ are presented in Figure 1c where the relative energies along the proposed diffusion paths are plotted against reaction coordinate corresponding to the migration distance from the initial state. The minimum energy path of the vacancy migration here is the straight line between the initial 8c octahedral site to the nearest neighbouring octahedral site. An octahedral → tetrahedral → octahedral path was also investigated, but it relaxed to the octahedral → octahedral path during cNEB calculations due to the unstable structure. The energetics of the Li vacancy along the same diffusion pathways is also presented for comparison. The energies of the initial and final states are identical and set to be 0 as reference. The energy barrier for the migration is defined as the energy difference between the saddle point, which is the highest point along the minimum energy path (MEP), and the initial state. For Mg diffusion, the energy barrier is 2.56 eV while that for Li is 0.97 eV. Such a high energy barrier, caused by the narrow channel for Mg diffusion, explains the sluggish diffusion of Mg cations compared with Li cations in the same host material.[1,2] Diffusion of Mg cations (or Li cations) in the host material also leads to a redistribution of charge around the moving ions. The planar charge difference ($\Delta\rho$ [e^-/$Bohr^{-3}$]) coordinate along the b-axis between a $MgMn_3O_4$

supercell with a vacancy at the initial state and at the saddle point (see Figure 1d) is shown in Figure 1e. The planar charge difference for $LiMn_3O_4$ is also shown for comparison. A substantial planar charge difference for a Mg vacancy migration is evident from the plots, and the relative charge difference between $MgMn_3O_4$ and $LiMn_3O_4$ reflects the dimensional difference of diffusion channels shown in Figure 1b. Therefore, it is reasonable to conclude that both the conversion reaction and the intercalation reaction could occur simultaneously on the surface of spinel Mn_3O_4, while further infiltration is expected to be hindered by kinetics due to the high diffusion barrier found by cNEB calculations. To gain a deeper understanding of the magnesiation process on the surface of Mn_3O_4, electrochemical measurements with a combination of STEM-EELS-EDS analysis are performed and discussed below.

Magnesiation mechanism and kinetics of the Mn_3O_4 cathode in APC-tetraglyme (G4) electrolyte. As shown in Figure S1, the galvanostatic charge/discharge measurements were first carried out on a cell configuration that consists of a Mn_3O_4 cathode (with Gif current collector), Mg counter electrode and APC-G4 electrolyte. The absence of the wide plateaus in the charge/discharge profiles of the Mn_3O_4 cathode at 15.4 mA g^{-1} (see Figure S1a) indicates no Mg intercalation into the bulk of the Mn_3O_4 nanoparticles. Instead, the nearly linear charge/discharge profiles suggest that the obtained reversible capacity, which is around 130 mAh g^{-1} at 15.4 mA g^{-1}, mainly originates from reactions occurring on the surface of the Mn_3O_4 nanoparticles, in line with the DFT calculations. Prior to reaching a relatively stable value, the Mn_3O_4 cathode experienced a decrease and subsequent increase of the capacity due to an activation effect on the electrode's surface during the initial magnesiation/de-magnesiation processes. Also, possible parasitic reactions, like Mn dissolution in the electrolyte,[40-42] may be lead to the capacity increase. Moreover, due to the fact that the magnesiation process of the Mn_3O_4 nanoparticles is limited by

surface kinetics, and not by solid-state ion diffusion, the Mn_3O_4 cathode shows excellent rate performance at various current densities from 15.4 mA g^{-1} to 1.54 A g^{-1} (see Figure S1b). The coulombic efficiencies stay at ~100% and capacities remain stable during the 5 cycles at each current density, except for the initial activation process at 15.4 mA g^{-1}. Importantly, there is no permanent capacity loss at 30.8 mA g^{-1} after cycling at a high current density of 1.54 A g^{-1}. However, for some reason, there is significant capacity decrease during the long-term cycling at 770 mA g^{-1}.

To further understand the charge storage mechanism of the Mn_3O_4 nanoparticles in APC-G4 electrolyte, a kinetics analysis according to the power-law relationship between the scan rate (v) and response current (i) from the CV curves (see Figure S2a), which is $i = av^b$ or $\log i = \log a + b \log v$ (both a and b are adjustable constants), is performed.[43] It is well-known that the response current of the active electrode originates from diffusion-controlled reactions (most typically intercalation reactions and conversion reactions) or/and non-diffusion controlled capacitive processes, typically the faradaic charge transfer with the surface/subsurface atoms, resulting in pseudocapacitance, and non-faradaic double-layer charging.[13-15,44,45] Both the diffusion and non-diffusion controlled behaviours can be identified by the *b*-values at fixed potentials (see Figure S2b and S2c). The *b*-values are determined from the slope of the linear plot of log i *vs.* log v shown in the insets of Figure S2b and S2c, and set to two well-defined values. The *b* approaches 0.5 for the reactions that are limited by ion diffusion, while a *b*-value close to 1 is expected for surface-dominated capacitive processes.[14,43] Hence, except for the low *b*-values for potentials below ~1.2 V during discharge (see Figure S2c), the high *b*-values for the major potentials both during charge (Figure S2b) and discharge (Figure S2c) suggest a non-diffusion controlled process to be more favoured for the Mn_3O_4 cathode during cycling. The contributions from the diffusion and non-

diffusion controlled processes can further be qualitatively quantified by dividing the response current (i) into the diffusion-controlled and non-diffusion controlled contribution at a fixed potential.[14,16] This is shown in Figure S2d, where it is clear that the capacitive contributions (~73%) are dominant in the Mn_3O_4 cathode. These results are in accordance with the sloping feature of the galvanostatic profiles (see inset in Figure S1a) and high *b*-values obtained during charge/discharge (see Figure S2b and S2c). Additionally, for a charge storage system governed by capacitive processes, the interfacial properties between electrode and electrolyte determine the cell performance, since the electron transfer and ion adsorption/diffusion occur at this interface. In order to investigate this charge transfer resistance more closely, EIS measurements were carried out on a two-electrode cell configuration, where Mn_3O_4 was used as working electrode and Mg metal as counter electrode. The fitted Nyquist plots of the Mn_3O_4 cathode are shown in Figure S2e and S2f. In the proposed equivalent circuit (see inset in Figure S2f), R_b is the bulk resistance of the cell, R_c is the charge transfer resistance of the cathode surface (corresponding to the semicircle at high frequency) and R_a is the charge transfer resistances of the anode surface (corresponding to the large semicircle at medium-low frequency).[46] Compared with the Mn_3O_4-APC-THF cell system ($Rc < 10\ \Omega$),[20] which is also governed by capacitive processes, the R_c values in the Mn_3O_4-APC-G4 cell are one order of magnitude higher. And also R_a values are much higher than other reported values in the APC-THF electrolyte (~15 kΩ).[46] The high R_c values indictate more sluggish kinetics for the charge transfer at the interface, for which also the capacity of the Mn_3O_4 cathode drops quickly during the initial cycles in Figure S1c. In order to further investigate the surface structure of the magnesiated Mn_3O_4 nanoparticles and also better understand the reasons for the high interfacial resistances and poor cycling stability, TEM was performed of both pristine and

cycled electrodes. High angle annular dark field (HAADF) STEM images (a-b), element maps (c-e) and the EEL Mn-$L_{2,3}$ peaks (f) are shown in Figure 2.

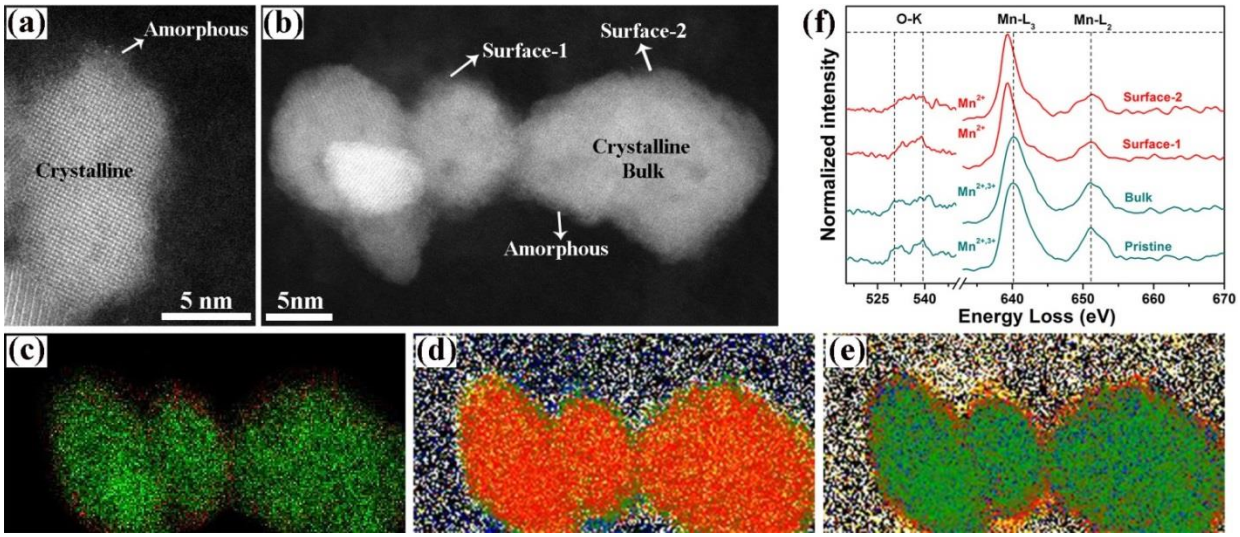

Figure 2. HAADF STEM images, EDS maps and EEL spectra of the magnesiated Mn_3O_4 cathode in APC-G4 electrolyte. (a,b) HAADF STEM images of the magnesiated Mn_3O_4 nanoparticles. (c) EDS map that combines the Mg and the Mn signal (Mn: green and Mg: red), quantified (d) Mn and (e) O maps from EELS. (f) The Mn-$L_{2,3}$ and O-K EEL edges of the pristine and the magnesiated Mn_3O_4 nanoparticles.

In the pristine Mn_3O_4 nanoparticles (see Figure S4) the crystal lattice clearly extends to the edges of the individual nanoparticles, and no amorphous layer can be observed. However, looking at Figures 2a and 2b, it is clear that an amorphous layer was formed on the surface of the cycled particles, while the bulk remains crystalline. The components of the surface layer was further analysed by EDS and EELS. In Figure 2c, the overlaid Mn-Mg map shows that Mg is primarily located on the surface of the cycled Mn_3O_4 nanoparticles. TEM is always two-dimensional projections, where the signal is averaged along the direction of the electron beam. Hence, what we here define as the bulk signal is not a pure bulk signal, but also has contributions from the top and

the bottom surfaces of the Mn_3O_4 nanoparticles. Even if the Mg is only located in a thin amorphous surface layer, a Mg signal should still be detected everywhere on the particle due to the loss of sensitivity along the electron beam direction. But the relative amount of Mg compared to other elements should be much higher at the edge of the projected nanoparticles. This behaviour is exactly what is observed in the element maps. Furthermore, quantification of every pixel in the EELS maps shows that the Mn concentration is significantly lower (Figure 2d) and the O concentration is significantly higher (Figure 2e) at the surface relative to the bulk. The Mg is therefore present as an oxide, and MgO is one possibility. In contrast to the Mg, the majority of the Mn is located in the bulk (see Figure 2c), resulting in a relatively higher Mn concentration in the bulk than that in the surface layer (see Figure 2d). To further analyse possible differences between bulk and surface located Mn, the fine structure of the EEL Mn-$L_{2,3}$ edges was studied. As shown in Figure 2f, the Mn-$L_{2,3}$ edges of the magnesiated Mn_3O_4 bulk are nearly identical to those of the pristine Mn_3O_4, implying that the Mn_3O_4 bulk remains unchanged during magnesiation. This is in line with the above DFT calculations, concluding that the crystalline structure of the bulk Mn_3O_4 should remain unchanged since Mg intercalation is hindered by high energy barriers for diffusion. However, the Mn-$L_{2,3}$ edges from the surface layer differs from those acquired from the bulk by several important fine structure changes: i) The Mn L_3 peak has a chemical shift with a change of the peak onset energy to lower energies at the surface. ii) The L_3/L_2 ratio is higher at the surface compared to the bulk. iii) The full width at half maximum (FWHM) of the L_3 peak decreases in the surface layer. All these changes in the Mn-$L_{2,3}$ fine structure are compatible with a reduction process where most of the Mn^{3+} is reduced to Mn^{2+}.[47,48] The differences seen in the O-K edges between spectra acquired at the surface and the bulk part of the magnesiated Mn_3O_4 are

more complex to interpret since several O-containing compounds contribute to the O signal at the surface.

Thus, based on the above discussion, a possible magnesiation mechanism of the Mn_3O_4 cathode in APC-G4 electrolyte is proposed as follows:

$Mg^{2+} + Mn_3O_4 + 2e^- \rightarrow (Mg^{2+}, Mn^{2+})O$ (surface) + $2/3Mn_3O_4$ (bulk)

This proposed conversion reaction on the surface of the Mn_3O_4 nanoparticles corresponds well with the DFT calculations. Although, one of the mechanisms proposed by DFT calculations has now been ruled out. Surface intercalation, which would form $MgMn_3O_4$, is not a possibility as this would give a crystalline product, and the surface layer observed here is clearly amorphous. This observed conversion reaction, which is limited by poor Mg diffusion along the surface of the Mn_3O_4 nanoparticles, is most likely irreversible since the regeneration of crystalline Mn_3O_4 from amorphous $(Mg^{2+}, Mn^{2+})O$ (surface) should be impossible. The amorphous layer formed by the conversion reaction could also passivate the active surface of the electrode as both MgO and MnO are insulators, which will inherently block the transfer of ions and electrons.[40] Such an amorphous layer may therefore explain the large charge transfer resistance observed at the interface of the Mn_3O_4 cathode and APC-G4 electrolyte (see Figure S2e). As a consequence, it is reasonable to conclude that the phase transformation on the surface of the Mn_3O_4 nanoparticles during magnesiation is the major cause for the capacity fading of the Mn_3O_4 cathode in APC-G4 electrolyte. Only ~70% of the initial capacity was retained after several hundred cycles, which is mainly the contribution from the capacitive effect, as ~70% of the total stored charge in Mn_3O_4 cathode comes from the capacitive contribution (see Figure S2d). The high interfacial resistance hinders the G4-related reactions at the electrode/electrolyte interface, resulting in the obtained capacity all coming from the capacitive contribution. Similar amorphous surface@crystalline bulk

morphology has been observed in a Mg battery with α-MnO_2 as cathode and [$Mg_2(\mu\text{-}Cl)_3 \cdot 6(OC_4H_8)$][$(N(Si(CH_3)_3)_2)_nAlCl_{4-n}$] (n = 1,2) electrolyte, according to work by Arthur *et al.*.[40] With the conversion mechanism, the initial capacity of α-MnO_2 is up to 280 mAh g^{-1}. However, the formation of an ion-blocking (Mg, Mn)O amorphous layer results in poor cycling stability, and ~70% of the initial capacity is lost after only 6 cycles.

Interestingly, in addition to the conversion reaction, the high O concentration and low Mn concentration in the surface layer of the cycled Mn_3O_4 nanoparticle indicate that there are other interfacial reactions going on as well. In the Mn_3O_4-APC-THF cell, the coordinated THF molecules in the Mg complex are involved in the interfacial reactions.[20] Thus, it is likely to believe that the coordinated G4 solvent molecules at the Mn_3O_4/APC-G4 interface are involved in and dominate the diffusion-controlled interfacial reactions. As Conway *et al.* explained in their work, the redox reactions can be limited by the ion diffusion if the redox reactants are solution species.[49] Nevertheless, revealing the details of the solvent-related interfacial reactions is still a work in progress due to the complexity of the APC electrolytes, and is beyond the scope of this work. Furthermore, as shown in Figure S5b-S5d, the features of the CV curves of Mn_3O_4 with metallic current collectors reveal that the response currents stem from capacitive processes (or in combination with small contributions from interfacial reactions involving the electrolyte species). Also here Mg intercalation can be excluded as there are no apparent redox peaks. However, the capacities obtained from pure Gif and the Mn_3O_4 cathode with the metallic current collectors (e.g. Cuf, Nif and SSf) are negligible (see Figure S5f) compared to that measured with the Mn_3O_4 cathode on the Gif current collector (see Figure S1a). The observed continuous incline in the CV curves of the Mn_3O_4 cathodes on metallic current collectors indicate high contact resistance between the active material and the current collector, which may explain the poor capacity

observed from these electrodes. The CV curves for the Mn_3O_4 cathode on Gif did not show this sloping behavior, indicating good adherence between the active material and the current collector.

In short, the interfacial reactions involving the G4 molecules facilitate conversion reactions on the surface of the Mn_3O_4 nanoparticles, but are associated with high interfacial resistances and poor cycling stability. These results indicate that conversion reactions of this form should be avoided. Also, the G4 solvent seems to play an important role in initiating these reactions. With this concern in mind, the ether solvent DME, with shorter molecular chain length relative to the G4 molecule ($(CH_3O(CH_2CH_2O)_nCH_3$ (n equals to 1 for DME, and 4 for G4)), has been investigated as solvent for the APC electrolyte. The electrochemical performance and magnesiation mechanism analysis of the Mn_3O_4 cathode in APC-DME electrolyte are discussed in the following section.

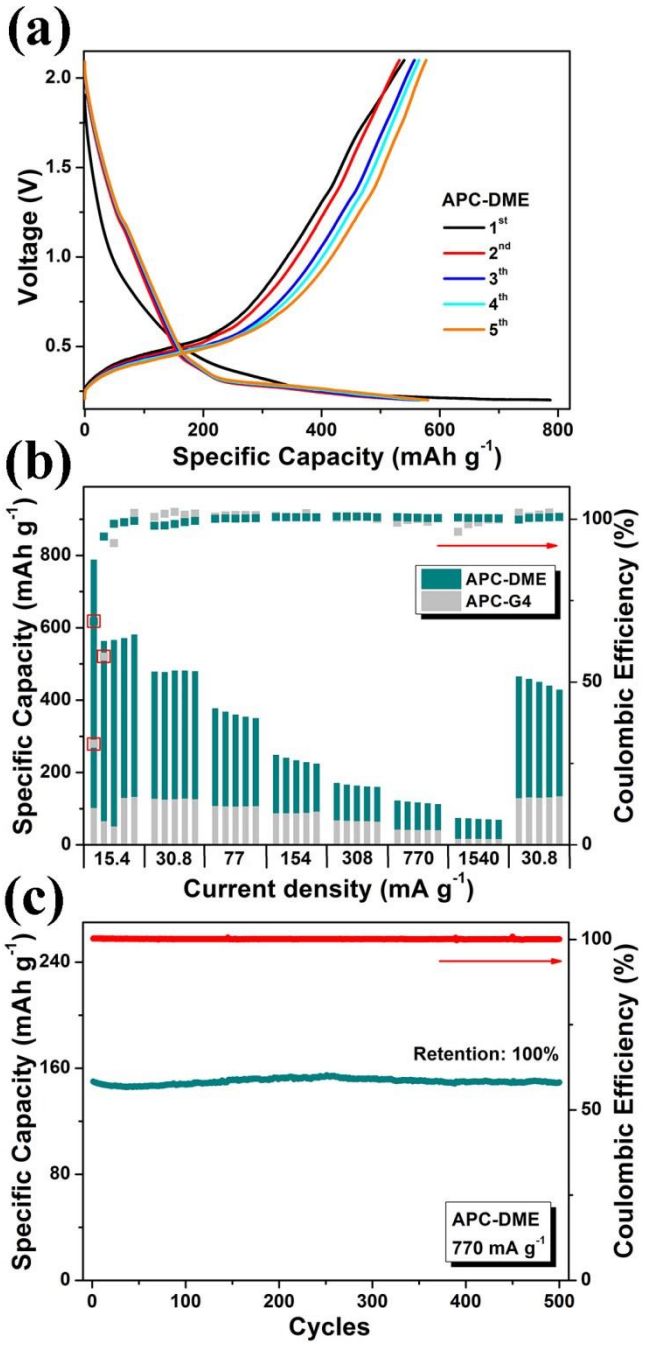

Figure 3. Electrochemical charge storage performance of the Mn_3O_4 cathode in APC-DME electrolyte. (a) Galvanostatic charge/discharge profiles at 15.4 mA g^{-1}. (b) Rate performance. (c) Long-term cycling at 770 mA g^{-1}.

Magnesiation mechanisms and kinetics of the Mn_3O_4 cathode in APC-DME electrolyte. The charge storage performance of the Mn_3O_4 cathode in APC-DME electrolyte is shown in Figure 3. Mn_3O_4 exhibits an extremely high initial capacity of ~800 mAh g^{-1} at 15.4 mA g^{-1} (see Figure 3a). There is a significant capacity loss after the first cycle, which may be caused by irreversible electrolyte decomposition during the initial magnesiation. However, Mn_3O_4 still exhibits a reversible capacity of ~580 mAh g^{-1} from the 2nd cycle onwards, which is more than 4 times the reversible capacity obtained in APC-G4 electrolyte. Relative to the moderate rate capability observed in the APC-G4 electrolyte, the capacities in the APC-DME electrolyte remain quite high at increased current rates, and with ~100% efficiencies (see Figure 3b). The long-term stability is also very good, and no capacity decay is observed after 500 cycles at 770 mA g^{-1} (see Figure 3c). Taking both the specific capacity and cycling stability into consideration, the charge storage performance of the Mn_3O_4 cathode is to the best of our knowledge, higher than any other materials reported thus far, including other oxides, silicates, sulphides, selenides, carbon allotropes and organic-based cathodes (see comprehensive comparison in Table S1). Based on the results obtained with other electrolytes, we can with certainty attribute the excellent electrochemical performance of the Mn_3O_4 cathode to the DME solvent. This also indicates that the magnesiation mechanism in the APC-DME electrolyte is different from that found in the APC-G4 electrolyte. The different features of the galvanostatic voltage profiles (see Figure 3a) and CV curves (see Figure S6d) in the APC-DME electrolyte also strongly suggest that this is the case. Based on the quantitative kinetic analysis of the Mn_3O_4 cathode in APC-DME electrolyte (see Figure S6a-S6d), this difference in the magnesiation mechanism becomes clear.

Compared with the narrow potential range that corresponds to the diffusion-controlled process in the APC-G4 electrolyte (below ~1.2 V in discharge), the diffusion-controlled reactions are more

favored both during charge (see Figure S6b) and discharge (see Figure S6c) in the APC-DME electrolyte. This is particularly evident for potentials around the redox peaks, where the low *b*-values indicate that the corresponding redox reactions are limited by ion diffusion.[14,45] As a result, 42% of the total stored charge is found to stem from redox reactions (see Figure S6d), which is significantly higher than the 27% calculated for the APC-G4 electrolyte (see Figure S2d). This result is also consistent with the sloping features of the charge/discharge profiles of the Mn_3O_4 cathode in the APC-DME electrolytes. In contrast to the nearly linear profiles observed for the APC-G4 electrolyte in Figure S1a, the discharge profiles in APC-DME electrolyte (see Figure 3a) exhibit a long and nearly flat plateau starting below ~0.3 V. It is these diffusion-controlled reactions that provide the extremely high capacity obtained for the Mn_3O_4 cathode when the DME solvent is used.

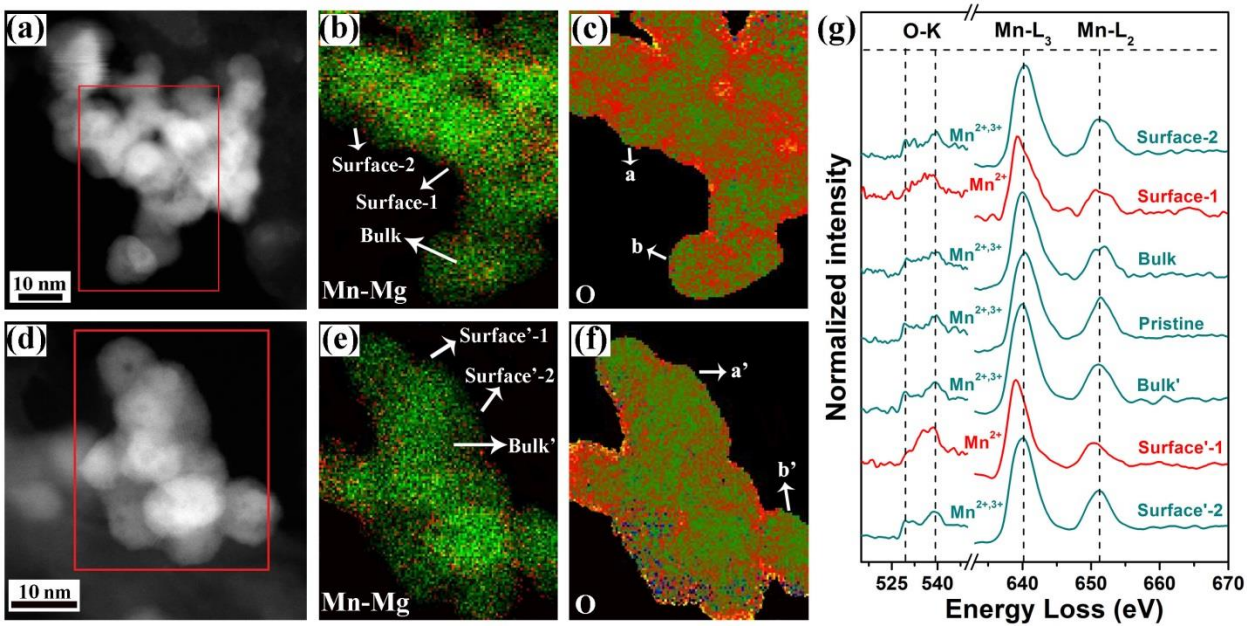

Figure 4. STEM images, EDS maps and EEL spectra of the magnesiated Mn_3O_4 cathode in APC-DME electrolyte. (a,d) HAADF STEM image, (b,e) EDS map that combines the Mg and the Mn signals (Mn: green and Mg: red). (c,f) The relative concentrations of O after quantification of every pixel in the EEL spectrum image. (g) The Mn-$L_{2,3}$ peaks of the magnesiated Mn_3O_4 nanoparticles.

Moreover, as shown in Figure S6e and S6f, the charge transfer resistances at the electrode/electrolyte interfaces in the APC-DME electrolyte are much smaller than that found in the APC-G4 electrolyte (see Figure S2e and S2f), which can be partially attributed to the shorter chain structure of the DME solvent. The low interfacial resistances are essential for the high charge storage performance of the electrode materials. Following the analysis method used for the magnesiated Mn_3O_4 in APC-G4 electrolyte, a more thorough study of the magnesiation mechanism of the Mn_3O_4 nanoparticles in the APC-DME electrolyte has been done by combining STEM imaging with EEL spectroscopy, and the results are shown in Figure 4. Similar to what was observed for the Mn_3O_4 particles cycled using the APC-G4 electrolyte, there is a clear enrichment

of Mg on the surface of the magnesiated Mn_3O_4 nanoparticles in APC-DME electrolyte (see Figure 4b and 4e). And, for the elemental dispersion on the major surface of the nanoparticles relative to the bulk, the Mn concentration is lower (see Figure S7) while the O concentration is higher (see Figure 4c and 4f). These variations in the concentration of the elements between the bulk and the surface are due to the formation of reaction products generated by the DME solvent interfacial reactions. EELS analysis show Mn-$L_{2,3}$ peaks compatible with pristine crystalline Mn_3O_4 when collected from the bulk, but the peak shift of Mn-L_3 edge to the low energy is observed for a small part of the Mn_3O_4 surface only, based on detailed analysis of changes in the fine structure of the Mn-$L_{2,3}$ peaks (see Surface-1 in Figure 4b, and Surface'-1 in Figure 4e). Hence, only small segregated parts of the Mn_3O_4 surface show indications of a conversion reaction. On the other hand, the major part of the Mn_3O_4 nanoparticle surface remains unaltered with respect to the electronic structure of the Mn (see Surface-2 in Figure 4b and Surface'-2 in Figure 4e). Note that, on the surface marked a and b in Figure 4c and Figure S7a, a' and b' in Figures 4f and Figure S7b, the O and Mn concentrations are the same as in the bulk. The variation in behavior of the Mn_3O_4 surface is most likely caused by variations in the reaction enthalpies of the interfacial reactions with different specific crystalline orientations on the surface of the Mn_3O_4 particles.[50-52] This implies differences in the interactions of the Mn_3O_4 surface with the Mg complexes.

Like the situations in both the Mn_3O_4-APC-G4 and the Mn_3O_4-APC-THF cell systems, also here the solvent-related interfacial reactions can only proceed in the presence of the Gif current collector (see Figure S8). The pure Gif displays similar features in the CV curve as Mn_3O_4-Gif (see Figure S8a). While the CV curves for the Mn_3O_4 cathode on metallic current collectors (see Figure S8b-S8d) exhibit more inclined rectangular features without any obvious redox peaks, which is caused by the high contact resistance between the electrode materials and the metallic

current collectors. In addition, the capacities obtained from the pure Gif and from the Mn_3O_4 cathodes on metallic current collectors are negligible. It can also be seen that the anodic peak in the CV curve of Mn_3O_4-Gif shifts to a lower potential compared with the same peak in the CV curve of pure Gif, which indicates a close relationship between the surface properties of the electrode materials and the solvent-related interfacial reactions. These DME-related interfacial reactions are highly reversible and provide a substantial capacity according to the galvanostatic cycling data shown in Figure 3.

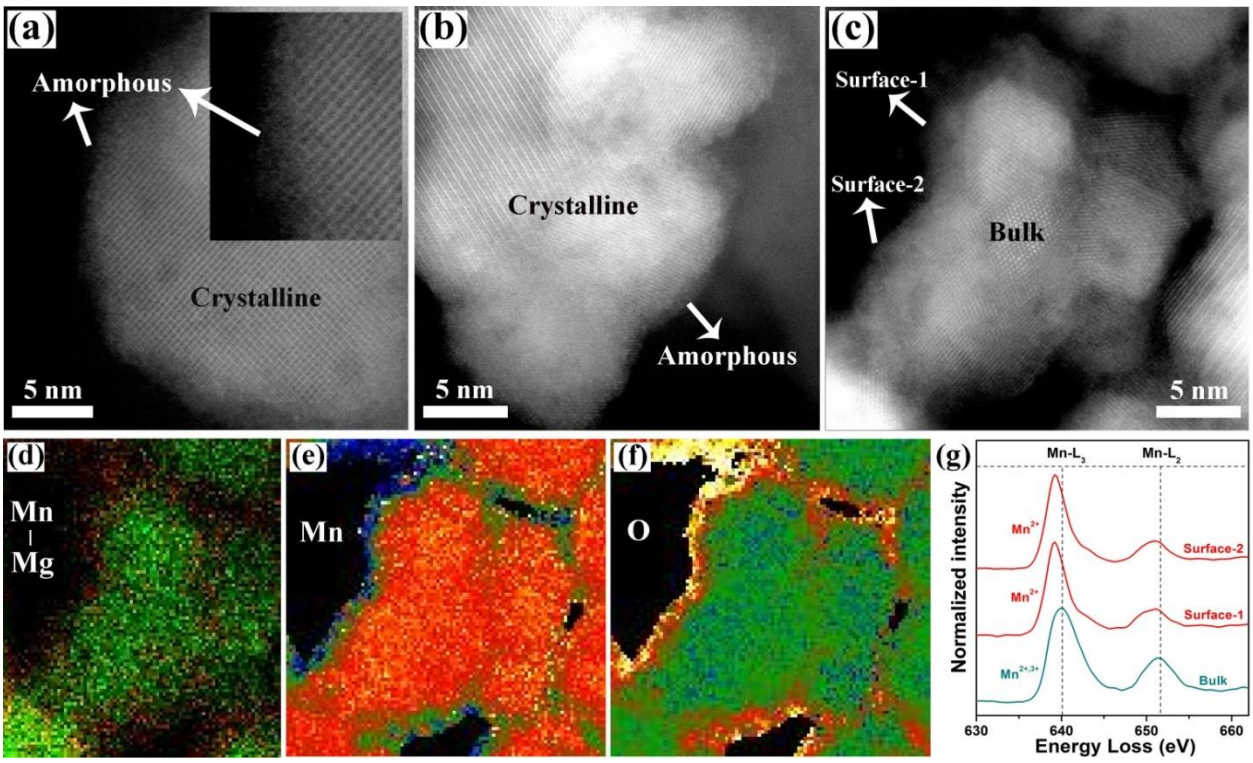

Figure 5. STEM images, EDS maps and EEL spectra of the magnesiated Mn_3O_4 anode in APC-DME electrolyte. (a-c) HAADF STEM images of the magnesiated Mn_3O_4 nanoparticles. (d) EDS map that combines the Mg and the Mn signals (Mn: green and Mg: red). (e) and (f) show the relative concentrations of Mn and O, respectively, after quantification of every pixel in the

EEL spectrum image. (g) The EEL Mn-$L_{2,3}$ peaks collected from the surfaces and from the bulk of the magnesiated Mn_3O_4 nanoparticles.

Magnesiation mechanism and kinetics of the Mn_3O_4 anode in APC-DME electrolyte. The behavior observed for the Mn_3O_4 cathode in APC-DME electrolyte, with a wide plateau around 0.2 V, indicates that the material may be equally promising as anode in a Mg battery rather than a cathode. The Mn_3O_4 nanoparticles cast on a Gif current collector was therefore cycled as an anode with lower cut-off potentials of 0.01-1 V. In Figure S9a, it can be seen that the Mn_3O_4 anode displays an initial capacity of ~2500 mAh g^{-1} with a reversible capacity of ~1800 mAh g^{-1} at 15.4 mA g^{-1} in the APC-DME electrolyte. This is to the best of our knowledge, by far the highest capacities measured among any reported electrodes for Mg batteries (including both the cathode and anode materials, see a comprehensive comparison in Table S1 and Table S2). When the current density was increased to 308 mA g^{-1}, the capacity was still ~500 mAh g^{-1} for the Mn_3O_4 anode (see Figure S9b). There is significant overlap between the potential windows used for anode and cathode discharge, more specifically between 1 and 0.2 V. It is therefore reasonable to assume that the discharge mechanisms in this voltage range are similar for the two cases, which means that diffusion-controlled reactions occur also at the Mn_3O_4 (anode)/electrolyte interface between about 1 and 0.2 V. However, for the anode the reactions are allowed to proceed much further, and at lower potentials the reactions may change. It is obvious that the capacity increases dramatically when extending the lower cut-off potential to 0.01 V. As a consequence, the fraction of the capacity contribution from the diffusion-controlled reactions in the Mn_3O_4 anode (64%) is significantly higher than that in the Mn_3O_4 cathode (42%). Figure S9c and Figure S10 show the results of the quantitative kinetic analysis of the Mn_3O_4 anode in APC-DME electrolyte. This enhanced contribution from the diffusion-controlled reactions, however, results in a poor cycling stability of

the Mn_3O_4 anode (see Figure S9d). After the initial 200 cycles at 770 mA g^{-1}, where 86% of the initial capacity is retained, the capacity decreased rapidly, and only 39% remains after 500 cycles. The reason for the poor cycling stability can be explained by the STEM-EDS-EELS characterizations of the Mn_3O_4 anode after 500 cycles at 770 mA g^{-1} (see Figure 5). Similar to what was observed for the magnesiated Mn_3O_4 nanoparticles in APC-G4 electrolyte (see Figure 2), an amorphous layer has formed on the surface of the magnesiated Mn_3O_4 nanoparticles in the APC-DME electrolyte (see Figure 5a-5c). According to the EDS maps (see Figure 5d and 5f) and Mn-L_3 edges spectra (see Figure 5g), the surface contains (Mg^{2+}, Mn^{2+})O, while the bulk remains as crystalline Mn_3O_4. This amorphous layer is caused by a conversion reaction, and solvent-related interfacial reactions (which may be irreversible at potentials close to 0.01 V) could account for the poor cycling stability of the Mn_3O_4 anode in APC-DME electrolyte.

To give a brief summary of the presented results, the high charge density of the Mg cations seems to cause partial desolvation of the Mg complexes at the interface, which greatly affects the charge transfer resistance during magnesiation. The Mg cations in the complex adsorb on the surface of the electrode, providing the capacitive contribution. The coordinated species are involved in the interfacial reactions. The interfacial reactions governed by the solvents of the APC electrolyte could significantly affect the surface activity of the electrode material, resulting in the large differences in electrochemical performance of the Mn_3O_4 cathode in APC-DME and APC-G4 electrolytes. Compared with the DME molecule, which has short chain-length and only one type of oxygen with respect to molecular symmetry, the long chain structured G4 molecule has three types of oxygen. This complicates the structures of its coordinated Mg complexes, which in turn affects the involved interfacial reactions. These complex interfacial reactions result in a phase transformation on the surface of the Mn_3O_4 nanoparticles and probably account for the high

interfacial resistances. In addition, the passivated surface of the Mn_3O_4 nanoparticles in APC-G4 electrolyte may greatly hinder the subsequent magnesiation processes, resulting in low capacities, which mainly stem from capacitive contributions. On the contrary, the interfacial reactions involving the short chain DME molecules are highly reversible, and lead to low interfacial resistances, since no phase change was observed for the major surface of the Mn_3O_4 nanoparticles. These reversible interfacial reactions are thus facilitated on the surface of the Mn_3O_4 nanoparticles and contributed to a substantial improvement in the discharge capacity.

CONCLUSIONS

This work has brought us one step closer to unraveling and understanding the mechanisms governing the high capacities observed in a new type of Mg battery. This is a battery where the capacity originates from capacitive processes and the interfacial reactions governed by the electrolyte solvent. The advantage of this type of battery over the conventional intercalation based Mg batteries is the circumvention of the sluggish Mg diffusion in a host lattice. By utilization of the reversible interfacial reactions involving the electrolyte solvents, Mn_3O_4 exhibits a reversible capacity of ~580 mAh g^{-1} as cathode, and ~1800 mAh g^{-1} reversible capacity as anode in APC-DME electrolyte. These extremely high capacities, together with the stable cycling performance (100% retention after 500 cycles at 770 mA g^{-1} for Mn_3O_4 cathode and 86% retention after the initial 200 cycles at 770 mA g^{-1} for Mn_3O_4 anode), represent a possibility to develop this new type of Mg battery with high charge storage performance as a substitute for intercalation based Mg batteries.

■ ASSOCIATED CONTENT

Supporting Information.

Experimental section. Electrochemical charge storage performance of the Mn_3O_4 cathode in APC-G4 electrolyte. Kinetics, quantitative and impedance analysis of the Mn_3O_4 cathodes in APC-G4 electrolyte. The plots of $v^{1/2}$ vs i $v^{-1/2}$. TEM image of the pristine Mn_3O_4 electrode. The comparison of CV curves of Mn_3O_4 cathode with different current collectors at 0.2 mV s^{-1} in APC-G4 electrolyte. Galvanostatic charge/discharge profiles of Mn_3O_4 cathode with different current collectors at 15.4 mA g^{-1} in APC-G4 electrolyte. Kinetics, quantitative and impedance analysis of the Mn_3O_4 cathode in APC-DME electrolyte. The relative concentrations of Mn after quantification of the EEL spectrum image. CV curves of Mn_3O_4-Cuf, Mn_3O_4-Nif, Mn_3O_4-SSf and pure Gif at 0.2 mV s^{-1} in APC-DME electrolyte. Galvanostatic charge/discharge profiles of Mn_3O_4 cathode with different current collectors at 15.4 mA g^{-1} in APC-DME electrolyte. Electrochemical charge storage performance and quantitative analysis of the Mn_3O_4 anode in APC-DME electrolyte. Dependence of *b*-values as a function of potential for anodic sweeps and cathodic sweeps. A survey of electrochemical performance of cathodes (or anodes) in Mg battery.

■ AUTHOR INFORMATION

Corresponding Author

*E-mail: fride.vullum-bruer@ntnu.no

Notes

The authors declare no competing financial interest.

■ ACKNOWLEDGMENT

This work was sponsored by the Research Council of Norway through the project NanoMag (Grant no. 221785). Computational resources were provided by the Norwegian Metacenter for Computational Science (NOTUR) through the project NN9264K and NTNU243.

■ REFERENCES

(1) Levi, E.; Gofer, Y.; Aurbach, D. *Chem. Mater.* **2010**, *22,* 860-868.

(2) Yoo, H. D.; Shterenberg, I.; Gofer, Y.; Gershinsky, G.; Pour, N.; Aurbach, D. *Energy Environ. Sci.* **2013**, *6,* 2265-2279.

(3) Muldoon, J.; Bucur, C. B.; Oliver, A. G.; Sugimoto, T.; Matsui, M.; Kim, H. S.; Allred, G. D.; Zajicek, J.; Kotani, Y. *Energy Environ. Sci.* **2012**, *5,* 5941-5950.

(4) Aurbach, D.; Lu, Z.; Schechter, A.; Gofer, Y.; Gizbar, H.; Turgeman, R.; Cohen, Y.; Moshkovich, M.; Levi, E. *Nature* **2000**, *407,* 724-727.

(5) Lancry, E.; Levi, E.; Gofer, Y.; Levi, M.; Salitra, G.; Aurbach, D. *Chem. Mater.* **2004**, *16,* 2832-2838.

(6) Liang, Y. L.; Feng, R. J.; Yang, S. Q.; Ma, H.; Liang, J.; Chen, J. *Adv. Mater.* **2011**, *23,* 640-643.

(7) Liu, Y. C.; Jiao, L. F.; Wu, Q.; Du, J.; Zhao, Y. P.; Si, Y. C.; Wang, Y. J.; Yuan, H. T. *J. Mater. Chem. A* **2013**, *1,* 5822-5826.

(8) Sun, X.; Bonnick, P.; Duffort, V.; Liu, M.; Rong, Z.; Persson, K. A.; Ceder, G.; Nazar, L. F. *Energy Environ. Sci.* **2016**, *9,* 2273-2277.

(9) Spahr, M. E.; Novak, P.; Haas, O.; Nesper, R. *J. Power Sources* **1995**, *54,* 346-351.

(10) Gershinsky, G.; Yoo, H. D.; Gofer, Y.; Aurbach, D. *Langmuir* **2013**, *29,* 10964-10972.

(11) Cheng, Y.; Shao, Y.; Raju, V.; Ji, X.; Mehdi, B. L.; Han, K. S.; Engelhard, M. H.; Li, G.; Browning, N. D.; Mueller, K. T.; Liu, J. *Adv. Funct. Mater.* **2016**, *26,* 3446-3453.

(12) An, Q.; Li, Y.; Deog Yoo, H.; Chen, S.; Ru, Q.; Mai, L.; Yao, Y. *Nano Energy* **2015**, *18,* 265-272.

(13) Augustyn, V.; Come, J.; Lowe, M. A.; Kim, J. W.; Taberna, P. L.; Tolbert, S. H.; Abruna, H. D.; Simon, P.; Dunn, B. *Nat. Mater.* **2013**, *12,* 518-522.

(14) Wang, J.; Polleux, J.; Lim, J.; Dunn, B. *J. Phys. Chem. C* **2007**, *111,* 14925-14931.

(15) Augustyn, V.; Simon, P.; Dunn, B. *Energy Environ. Sci.* **2014**, *7,* 1597.

(16) Chao, D.; Zhu, C.; Yang, P.; Xia, X.; Liu, J.; Wang, J.; Fan, X.; Savilov, S. V.; Lin, J.; Fan, H. J.; Shen, Z. X. *Nat. Commun.* **2016**, *7,* 12122.

(17) Xie, J.; Li, C.; Cui, Z.; Guo, X. *Adv. Funct. Mater.* **2015**, *25,* 6519-6526.

(18) Zhang, Y.; Xie, J.; Han, Y.; Li, C. *Adv. Funct. Mater.* **2015**, *25,* 7300-7308.

(19) Zhang, R.; Yu, X.; Nam, K.-W.; Ling, C.; Arthur, T. S.; Song, W.; Knapp, A. M.; Ehrlich, S. N.; Yang, X. Q.; Matsui, M. *Electrochem. Commun.* **2012**, *23,* 110-113.

(20) Wang, L.; Asheim, K.; Vullum, P. E.; Svensson, A. M.; Vullum-Bruer, F. *Chem. Mater.* **2016**, *28,* 6459-6470.

(21) Bucur, C. B.; Gregory, T.; Oliver, A. G.; Muldoon, J. *J. Phys. Chem. Lett.* **2015**, *6,* 3578-3591.

(22) Benmayza, A.; Ramanathan, M.; Arthur, T. S.; Matsui, M.; Mizuno, F.; Guo, J.; Glans, P. A.; Prakash, J. *J. Phys. Chem. C* **2013**, *117,* 26881-26888.

(23) Canepa, P.; Gautam, G. S.; Malik, R.; Jayaraman, S.; Rong, Z.; Zavadil, K. R.; Persson, K.; Ceder, G. *Chem. Mater.* **2015**, *27,* 3317-3325.

(24) Wan, L. W. F.; Perdue, B. R.; Apblett, C. A.; Prendergast, D. *Chem. Mater.* **2015**, *27,* 5932-5940.

(25) Mizrahi, O.; Amir, N.; Pollak, E.; Chusid, O.; Marks, V.; Gottlieb, H.; Larush, L.; Zinigrad, E.; Aurbach, D. *J. Electrochem. Soc.* **2008**, *155,* A103-A109.

(26) Barile, C. J.; Spatney, R.; Zavadil, K. R.; Gewirth, A. A. *J. Phys. Chem. C* **2014**, *118,* 10694-10699.

(27) Barile, C. J.; Barile, E. C.; Zavadil, K. R.; Nuzzo, R. G.; Gewirth, A. A. *J. Phys. Chem. C* **2014**, *118,* 27623-27630.

(28) Sommovigo, M.; Alper, H. *J. Mol. Catal.* **1994**, *88,* 151-158.

(29) Fazlurrahman, A. K.; Tsai, J. C.; Nicholas, K. M. *J. Chem. Soc. Chem. Comm.* **1992**, 1334-1335.

(30) Metsger, L.; Bittner, S. *Tetrahedron* **2000**, *56,* 1905-1910.

(31) Wang, T. J.; Ma, Z. H.; Huang, M. Y.; Jiang, Y. Y. *Polym. Adv. Technol.* **1996**, *7,* 88-91.

(32) Nguyen, D. T.; Tran, X. M.; Kang, J.; Song, S. W. *ChemElectroChem* **2016**, *3,* 1813-1819.

(33) Avgousti, C.; Georgolios, N.; Kyriacou, G.; Ritzoulis, G. *Electrochim. Acta* **1999**, *44,* 3295-3301.

(34) Pour, N.; Gofer, Y.; Major, D. T.; Aurbach, D. *J. Am. Chem. Soc.* **2011**, *133,* 6270-6278.

(35) Mizuno, F.; Singh, N.; Arthur, T. S.; Fanson, P. T.; Ramanathan, M.; Benmayza, A.; Prakash, J.; Liu, Y. S.; Glans, P. A.; Guo, J. *Front. Energy Res.* **2014**, *2*, 46-56.

(36) Dwight, K.; Menyuk, N. *Phys. Rev.* **1960**, *119,* 1470-1479.

(37) Tackett, R.; Lawes, G.; Melot, B. C.; Grossman, M.; Toberer, E. S.; Seshadri, R. *Phys. Rev. B* **2007**, *76*, 024409.

(38) Okamoto, S.; Ichitsubo, T.; Kawaguchi, T.; Kumagai, Y.; Oba, F.; Yagi, S.; Shimokawa, K.; Goto, N.; Doi, T.; Matsubara, E. *Adv. Sci.* **2015**, *2,* 1500072.

(39) Canepa, P.; Gautam, G. S.; Hannah, D. C.; Malik, R.; Liu, M.; Gallagher, K. G.; Persson, K. A.; Ceder, G. *Chem. Rev.* **2017**, *117*, 4287-4341.

(40) Arthur, T. S.; Zhang, R.; Ling, C.; Glans, P. A.; Fan, X.; Guo, J.; Mizuno, F. *ACS Appl. Mater. Interfaces* **2014**, *6,* 7004-7008.

(41) Sun, X. Q.; Duffort, V.; Mehdi, B. L.; Browning, N. D.; Nazar, L. F. *Chem. Mater.* **2016**, *28*, 534-542.

(42) Zhang, R. Q.; Arthur, T. S.; Ling, C.; Mizuno, F. *J. Power Sources* **2015**, *282,* 630-638.

(43) Lindstrom, H.; Sodergren, S.; Solbrand, A.; Rensmo, H.; Hjelm, J.; Hagfeldt, A.; Lindquist, S. E. *J. Phys. Chem. B* **1997**, *101,* 7717-7722.

(44) Simon, P.; Gogotsi, Y.; Dunn, B. *Science* **2014**, *343,* 1210-1211.

(45) Sathiya, M.; Prakash, A. S.; Ramesha, K.; Tarascon, J. M.; Shukla, A. K. *J. Am. Chem. Soc.* **2011**, *133,* 16291-16299.

(46) Tian, H.; Gao, T.; Li, X.; Wang, X.; Luo, C.; Fan, X.; Yang, C.; Suo, L.; Ma, Z.; Han, W.; Wang, C. *Nat. Commun.* **2017**, *8,* 14083.

(47) Laffont, L.; Gibot, P. *Mater. Charact.* **2010**, *61,* 1268-1273.

(48) Tan, H. Y.; Verbeeck, J.; Abakumov, A.; Van Tendeloo, G. *Ultramicroscopy* **2012**, *116,* 24-33.

(49) Conway, B. E.; Birss, V.; Wojtowicz, J. *J. Power Sources* **1997**, *66,* 1-14.

(50) Salazar-Alvarez, G.; Sort, J.; Surinach, S.; Baro, M. D.; Nogues, J. *J. Am. Chem. Soc.* **2007**, *129,* 9102-9108.

(51) Jarosch, D. *Miner Petrol* **1987**, *37,* 15-23.

(52) Wang, N.; Guo, L.; He, L.; Cao, X.; Chen, C. P.; Wang, R. M.; Yang, S. H. *Small* **2007**, *3,* 606-610.

Table of content